

Dust polarization modelling at large scale over the northern Galactic cap using EBHIS and *Planck* data

Debabrata Adak^{*1}, Tuhin Ghosh^{**2}, Francois Boulanger³, Urmas Haud⁴, Peter Kalberla⁵, Peter G. Martin⁶,
Andrea Bracco³, Tarun Souradeep^{1,7}

¹ Inter University Centre for Astronomy and Astrophysics, Post Bag 4, Ganeshkhind, Pune-411007, India

² School of Physical Sciences, National Institute of Science Education and Research, HBNI, Jatni 752050, Odisha, India

³ Laboratoire de Physique de l'École Normale Supérieure, ENS, Université PSL, CNRS, Sorbonne Université, Université de Paris, F-75005 Paris, France

⁴ Tartu Observatory, 61602 Tõravere, Tartumaa, Estonia

⁵ Argelander-Institut für Astronomie, Universität Bonn, Auf dem Hügel 71, D-53121 Bonn, Germany

⁶ CITA, University of Toronto, 60 St. George St., Toronto, ON M5S 3H8, Canada

⁷ Indian Institute of Science Education and Research, Dr. Homi Bhabha Road, Ward No. 8, NCL Colony, Pashan, Pune-411008, Maharashtra, India

June 18, 2020

ABSTRACT

The primary source of systematic uncertainty in the quest for the B -mode polarization of the Cosmic Microwave Background (CMB) introduced by primordial gravitational waves is polarized thermal emission from Galactic dust. Therefore, accurate characterization and separation of the polarized thermal dust emission is an essential step in distinguishing such a faint CMB B -mode signal. We provide a modelling framework to simulate polarized thermal dust emission based on the model described in Ghosh et al. (2017), making use of both the *Planck* dust and Effelsberg-Bonn HI surveys over the northern Galactic cap. Our seven-parameter dust model, incorporating both HI gas in three different column density templates as a proxy for spatially variable dust intensity and a phenomenological model of Galactic magnetic field, is able to reproduce both 1- and 2-point statistics of the observed dust polarization maps seen by *Planck* at 353 GHz over a selected low-column density region in the northern Galactic cap. This work has important applications in assessing the accuracy of component separation methods and in quantifying the confidence level of separating polarized Galactic emission and the CMB B -mode signal, as is needed for ongoing and future CMB missions.

Key words. Interstellar medium: dust, observations – ISM: structure – ISM: magnetic fields – polarization

1. Introduction

Gravitational waves, possibly generated during the inflation epoch introduce B -mode polarization in the cosmic microwave background (CMB; Starobinskij 1979; Fabbri & Pollock 1983). The measurement of this primordial CMB B -mode signal is the intense focus of ongoing and proposed CMB experiments. Galactic polarized foregrounds, especially polarized thermal dust emission (Martin 2007; Draine & Fraise 2009; Vaillancourt & Matthews 2012; Planck Collaboration Int. XXII 2015; Ashton et al. 2018; Planck Collaboration XII 2018), also produce a B -mode signal at microwave frequencies (Planck Collaboration Int. XXX 2016; Planck Collaboration XI 2018). Accurate modelling and separation of polarized dust emission is therefore a necessary step in the detection of a primordial CMB B -mode signal. Residual foregrounds due to imperfect component sep-

aration can be misinterpreted as detection of primordial CMB B -modes (Remazeilles et al. 2016).

Polarized thermal dust emission is expected from aspherical grains aligned with respect to the local Galactic magnetic field (GMF; Stein 1966). Many distinct mechanisms have been elaborated to account for the alignment of dust grains, starting from the first quantitative approach by Davis & Greenstein (1951); for a review, see Lazarian (2007) and Andersson et al. (2015).

Empirically, the all-sky map of dust polarization from *Planck* at 353 GHz (Planck Collaboration I 2016) reveals a connection between the dust intensity structures and the local orientation of the GMF projected on the plane of the sky (B_{POS}) (Planck Collaboration Int. XXXII 2016; Planck Collaboration Int. XXXV 2016). In the low-column-density or diffuse interstellar medium (ISM), the orientation of the dust intensity structures is observed to be preferentially parallel to B_{POS} (Planck Collaboration Int. XXXII 2016). Going to high-column-density regions, including star-forming molecular clouds, the preferred orientation of the dust intensity structures changes from parallel to perpendicular

* Corresponding author: debabrata@iucaa.in

** Corresponding author: tghosh@niser.ac.in

(Planck Collaboration Int. XXXV 2016; Soler et al. 2017; Jow et al. 2018). This change in relative orientation was predicted using sub- and trans-Alfvénic magnetohydrodynamic (MHD) simulations (Soler et al. 2013), and highlights the role of the magnetic field during the formation of the molecular clouds.

Away from the Galactic plane, *Planck* polarization maps reveal a large scatter in the distributions of the polarization fraction, p , and the polarization angle, ψ (Planck Collaboration Int. XIX 2015). A comparison with maps computed from a simulation of MHD turbulence in Planck Collaboration Int. XX (2015) shows that the large scatter of p is associated with variations in the orientation of the GMF along the line of sight (LOS), causing a depolarization effect. The simulation also reproduces the inverse relationship between p and polarization angle dispersion function, S (Planck Collaboration Int. XIX 2015). Subsequently, Planck Collaboration Int. XLIV (2016) connected the distributions of p and ψ with the amplitude of turbulent magnetic field using a phenomenological model. This model is discussed further and compared with the *Planck* data in Planck Collaboration XII (2018).

The *Planck* maps were also used to measure power spectra of dust polarization. At intermediate and high Galactic latitudes, in the multipole range, $40 < \ell < 600$, the ratio of dust EE to BB power (D_ℓ^{EE}/D_ℓ^{BB}) is found to be around 2 (Planck Collaboration Int. XXX 2016; Planck Collaboration XI 2018). Planck Collaboration Int. XXXVIII (2016) show that both the E - B power asymmetry and the correlation between dust temperature and E mode polarization, i.e. the dust TE correlation, can be accounted for by the alignment between the orientation of the filamentary structure of interstellar matter in the diffuse ISM, as traced by total dust emission, and the orientation of the GMF, as inferred from dust polarization (Planck Collaboration Int. XXXII 2016; Planck Collaboration Int. XXXVIII 2016). Caldwell et al. (2017) and Kandel et al. (2018) investigated whether these observed properties could be related to turbulence in the magnetised ISM, considering the contributions from slow, fast, and Alfvén MHD modes. Caldwell et al. (2017) conclude that the E - B power asymmetry and positive TE correlation cannot both be accounted for with their model. Using the same theoretical framework, Kandel et al. (2017) and Kandel et al. (2018) reached the opposite conclusion, assuming that any correlation between the gas density and the magnetic field is negligible. However, this assumption is challenged by the above-mentioned observed alignment between the filamentary structure and the magnetic field. Filamentary structures identified in HI 21-cm line spectroscopic data cubes, which were shown to trace density structure in the cold neutral medium (CNM) (Clark et al. 2019), are also found to be aligned with the GMF (Clark et al. 2014; Clark et al. 2015; Martin et al. 2015; Kalberla et al. 2016). Furthermore, Clark (2018) reported a correlation between the polarization fraction, p , and the degree of coherence of the orientation of HI emission features along the LOS, later used by Clark & Hensley (2019) to model dust polarization. Clearly, HI data contain valuable information on the structure of the GMF in the neutral atomic ISM.

Ghosh et al. 2017 (hereafter TG17) present a phenomenological model of dust polarization. This TG17 model combines the framework introduced by Planck Collaboration Int. XLIV (2016) with a decomposition of HI emission data into three distinct maps of HI column density referred to as ‘HI templates’. By adjusting just a few parameters, the TG17 model reproduces the one- and two-point statistical properties of dust polarization over that fraction of the southern Galactic cap (defined by the region of $b \leq -30^\circ$) where dust and HI emission are well corre-

lated. In this paper, we use this framework to fit the *Planck* PR3 data (Planck Collaboration I 2018) over a fraction of the northern Galactic cap at $b \geq 30^\circ$. The main goal is to extend the sky area available to fit and test the TG17 model.

This paper is organised as follows. In Sect. 2, we describe the data used from *Planck* and the Effelsberg-Bonn HI Survey (EBHIS). Section 3 describes the choice of sky region and HI templates used in our analysis. We summarise the statistical properties of the dust polarization over the selected region in Sect. 4. In Sect. 5, we briefly describe the phenomenological modelling framework. Section 6 describes how the model parameters were evaluated. We present separate aspects of the results in Sects. 7 and 8. Finally, we summarise our results in Sect. 9. In Appendix A, we explore a model based on alternative HI templates.

2. Datasets used

2.1. *Planck* dust polarization maps

In this paper, we use publicly available *Planck* PR3 data¹ (Planck Collaboration I 2018) at 353 GHz to study the statistical properties of the dust polarization. These maps are produced using only the polarization-sensitive bolometers (PSBs) and are expressed in thermodynamic temperature units (K_{CMB} , Planck Collaboration III 2018). We also use various subsets of the *Planck* polarization data at 353 GHz, namely, the half-mission maps (HM1 and HM2), yearly surveys (Y1 and Y2), and odd and even surveys (O and E) to debias the effect of instrumental noise (Sect. 4).

For dust intensity, we use the generalised needlet internal linear combination (GNILC) processed Stokes I map (Planck Collaboration IV 2018). *Planck* does not have the ability to measure absolute emission, and so it is necessary to correct for the zero level of the dust intensity map. By construction, the GNILC dust intensity map has a cosmic infrared background (CIB) monopole contribution of $452 \mu\text{K}_{\text{CMB}}$ at 353 GHz, which needs to be subtracted (Planck Collaboration III 2018). To correct for the Galactic HI offset and the contribution from dust emission associated with HII emission (Planck Collaboration XII 2018), a ‘fiducial’ offset of $63 \mu\text{K}_{\text{CMB}}$ is added back to the CIB-subtracted GNILC dust intensity map (hereafter, we refer to this final map as I_{G353}). The fiducial offset has an uncertainty of $40 \mu\text{K}_{\text{CMB}}$, with an associated ‘low’ and ‘high’ offset of $23 \mu\text{K}_{\text{CMB}}$ and $103 \mu\text{K}_{\text{CMB}}$, respectively.

The *Planck* Stokes Q and U maps at 353 GHz have a beam resolution of $4'.82$ (FWHM), and the I_{G353} map has the beam resolution of $5'$ (FWHM). To increase the signal-to-noise ratio, we smooth the dust Stokes I , Q , and U maps to a common resolution of $60'$ or $80'$ (FWHM) and reproject on the HEALPix grid² (Górski et al. 2005) with $N_{\text{side}} = 128$. To compare our dust model with the *Planck* data, we work with the $60'$ (FWHM) smoothed maps. However, to study the inverse relationship between S and p (Sect. 8) we work with $80'$ (FWHM) smoothed *Planck* data.

¹ <http://www.cosmos.esa.int/web/planck/pla>

² <https://healpix.jpl.nasa.gov>

2.2. EBHIS and HI4PI HI data

We use HI 21-cm line spectroscopic data from EBHIS³ (Kerp et al. 2011; Winkel, B. et al. 2016), which mapped the Milky Way gas in the northern Galactic sky with the 100 m telescope at Effelsberg. The survey has an angular resolution of 10.8 (FWHM), spectral resolution $\delta v = 1.44 \text{ km s}^{-1}$ (FWHM), and rms brightness temperature uncertainty of 90 mK. Velocities are with respect to the local standard of rest (LSR). The EBHIS data are projected on a HEALPix grid with $N_{\text{side}} = 1024$ ($\theta_{\text{pix}} = 3.4$). The EBHIS data also form the northern part of the all-sky product HI4PI (HI4PI Collaboration et al. 2016).

For optically thin emission, the total HI column density (N_{HI}) can be obtained by integrating the brightness temperature (T_b) over velocity channels (Wilson et al. 2009):

$$N_{\text{HI}} = 1.82 \times 10^{18} \times \int T_b dv \text{ cm}^{-2}. \quad (1)$$

3. Exploiting the HI data

3.1. Region selection

We describe the procedure to select the low-column-density region in the northern Galactic cap in which HI and dust emission are highly correlated, making HI a good proxy for dust.

Ultraviolet observations of molecular hydrogen, H_2 (Savage et al. 1977; Gillmon et al. 2006) and early results from *Planck* (Planck Collaboration XXIV 2011) show that dust emission associated with gas in the form of H_2 becomes significant for sight lines where the total N_{H} exceeds $4 \times 10^{20} \text{ cm}^{-2}$ (Arendt et al. 1998). Therefore, we restrict ourselves to the sky region in which $N_{\text{HI},50}$ is below a threshold $3.8 \times 10^{20} \text{ cm}^{-2}$, where $N_{\text{HI},50}$ from Eq. (1) is evaluated over the restricted velocity interval $|v| \leq 50 \text{ km s}^{-1}$. We explored extending the range up to 80 km s^{-1} and because there is little additional gas in this range our results below from the modelling analysis (Sects. 6 to 8) are robust. We also get the same model parameters for regions restricted by $N_{\text{HI},50}$ thresholds in the range $3.4 - 4.0 \times 10^{20} \text{ cm}^{-2}$. The sky fraction increases beneficially with threshold, but not significantly beyond the adopted $3.8 \times 10^{20} \text{ cm}^{-2}$. However, the model parameters change significantly for thresholds above $4 \times 10^{20} \text{ cm}^{-2}$, presumably because of the increased and unaccounted molecular fraction.

We build our mask using an iterative correlation analysis method as described in Planck Collaboration Int. XVII (2014). The initial mask contains unmasked pixels for which both the EBHIS and *Planck* data are available over the northern Galactic cap. At each iteration, we compute the linear correlation between I_{G353} and total N_{HI} over unmasked pixels of the binary mask produced in the previous iteration. We compute residuals by subtracting the fit to the correlation from the observed dust emission for each unmasked pixel and find the standard deviation (σ_{cg}) characterising the Gaussian core of these residuals (Fig. 1).

Next, the binary mask is updated by masking pixels for which the absolute value of the residual is greater than $3\sigma_{cg}$. A stable mask is obtained after five iterations, a region of 5900 deg^2 comprising 65% of the northern Galactic cap ($b \geq 30^\circ$), as shown in Fig. 2.

Hereafter we refer to this region as mask65. For later analysis, we apodize this binary mask by convolving it with a Gaussian window function of 2° (FWHM). After apodization, we

³ EBHIS data are available at <http://cdsarc.u-strasbg.fr/viz-bin/qcat?J/A+A/585/A41>

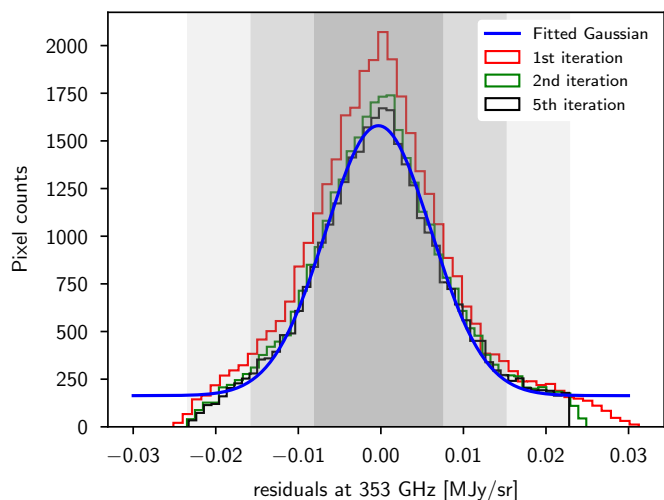


Fig. 1. Histogram of residuals at different iterations. The blue curve is the Gaussian fitted to residuals at the final iteration. Gray shaded regions are $1\sigma_{cg}$, $2\sigma_{cg}$, and $3\sigma_{cg}$ regions of the fitted Gaussian.

have an effective sky fraction, $f_{\text{sky}}^{\text{eff}}$, of 0.143 (14.3%). In the stable mask, there are some isolated islands with very few pixels. When we derive the full-sky angular power spectrum C_ℓ from the pseudo-spectrum, these isolated islands introduce correlations from very high ℓ to low ℓ via the mode-mode coupling matrix (Hivon et al. 2002). In our analysis, we eliminate isolated islands containing less than 20 pixels using the `Process_mask` routine of HEALPix.

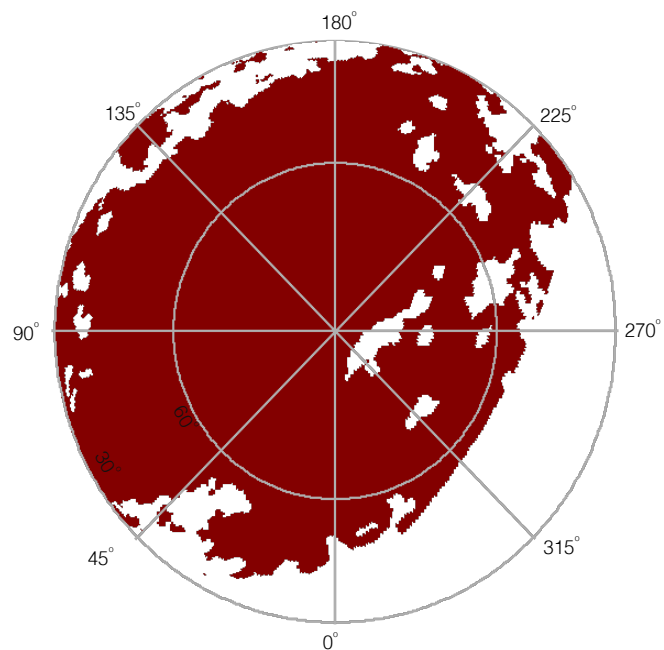


Fig. 2. Binary mask defining mask65, the dark regions selecting 65% of the northern Galactic cap ($b \geq 30^\circ$).

Over mask65 the mean HI column density over the restricted velocity interval is $\langle N_{\text{HI},50} \rangle = 1.85 \times 10^{20} \text{ cm}^{-2}$ and the mean dust intensity is $\langle I_{G353} \rangle = 293 \mu\text{K}_{\text{CMB}}$ at 353 GHz. The linear correlation between I_{G353} and total N_{HI} yields a slope or emissivity $\epsilon_{353,50}$ of $137 \mu\text{K}_{\text{CMB}} (10^{20} \text{ cm}^{-2})^{-1}$, where again the subscript 50 denotes the restricted velocity interval. This value

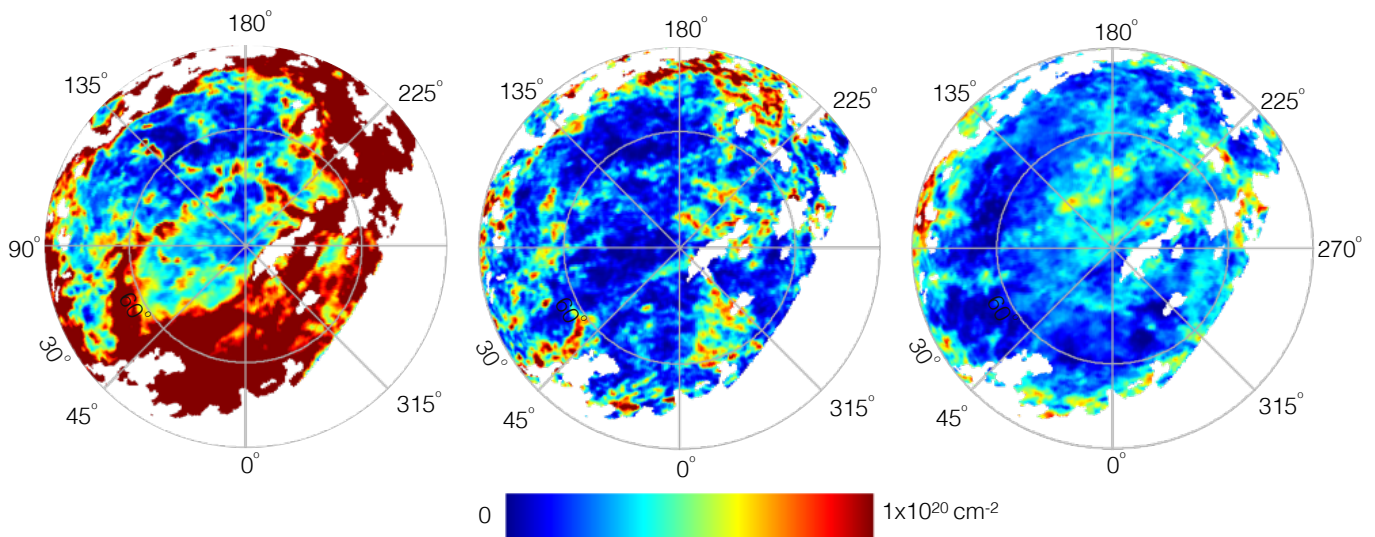


Fig. 3. Northern Galactic orthographic projection of integrated HI emission maps of the three HI templates called CNM (*left panel*), UNM (*middle panel*), and WNM (*right panel*). Over our selected region mask65 (Sect. 3.1), the mean column densities of the three templates are $\langle N_{\text{HI}}^{\text{c}} \rangle = 0.90 \times 10^{20} \text{ cm}^{-2}$, $\langle N_{\text{HI}}^{\text{u}} \rangle = 0.32 \times 10^{20} \text{ cm}^{-2}$, and $\langle N_{\text{HI}}^{\text{w}} \rangle = 0.56 \times 10^{20} \text{ cm}^{-2}$, respectively.

is about 2% higher than that found for the diffuse sky studied by [Planck Collaboration XI \(2014\)](#). The offset of $40 \mu\text{K}_{\text{CMB}}$ is satisfactory, within the systematic uncertainty of the zero level (Sect. 2.1).

3.2. HI templates

The diffuse ISM is a complex turbulent multiphase medium. The HI gas comprises two thermally stable phases, the cold and warm neutral medium (CNM and WNM, respectively), along with an additional thermally unstable phase at an intermediate temperature, hereafter referred to as the unstable neutral medium (UNM) following TG17.

HI spectra can be used to build maps of HI emission associated notionally with the CNM, UNM, and WNM. First, the observed brightness temperature profiles of HI spectra are decomposed into Gaussian components ([Haud 2000, 2013](#)) under the assumption that the random velocities in any HI ‘cloud’ have a Gaussian distribution. Thus,

$$T_{\text{b}}(v) = \sum_i T_0^i \exp \left[-\frac{1}{2} \left(\frac{v_{\text{LSR}} - v_c^i}{\sigma^i} \right)^2 \right], \quad (2)$$

where the summation is over all Gaussian components needed to describe the profile along a LOS, v_{LSR} is the velocity of the HI gas, and T_0^i , v_c^i , and σ^i are the peak brightness temperature (expressed in Kelvin), central peak velocity, and 1σ standard deviation of Gaussian component i , respectively.

Following the detailed physically motivated prescription in section 2.2 of TG17, we produce CNM, UNM, and WNM column density maps. This involves using weight factors applied in summing the contributions from the Gaussian components. The weights involve two parameters of the polarization model of TG17 that constrain the range of centroid velocities of the Gaussians that contribute to each of the three maps. Here we simply adopt the TG17 values for these two parameters and the same weighting scheme, which should not be materially different in the north as compared to the south. TG17 noted the beneficial effect of having considerable column density in the three maps

and that although the CMN contains some higher velocity dispersion gas, subdivision into two has little effect on the model. As we show below, this prescription does indeed lead to an acceptable polarization model for mask65.

These three maps have an original resolution of $10/8$ (FWHM), which we have smoothed to a common resolution of $60'$ (FWHM) at $N_{\text{side}} = 128$. The resulting maps, to be used as HI templates below, are shown in Fig. 3. In Appendix. A, we present an analysis that uses alternative HI templates based on a decomposition by [Kalberla & Haud \(2018\)](#).

4. Observed statistics from *Planck* dust observations over the selected region

In this section, we analyse the statistical properties of dust polarization over mask65 in both pixel and harmonic space.

4.1. Polarization fraction

To avoid a bias from data noise, we compute the square of the polarization fraction (p_{d}^2) combining independent subsets of the *Planck* data at 353 GHz:

$$p_{\text{d}}^2 = \left\langle \frac{Q_{\text{d}}^{s_1} Q_{\text{d}}^{s_2} + U_{\text{d}}^{s_1} U_{\text{d}}^{s_2}}{I_{G353}^2} \right\rangle, \quad (3)$$

where ‘d’ stands for the *Planck* data, (s_1, s_2) stands for different subsets of *Planck* data at 353 GHz: $\{(\text{HM1}, \text{HM2}); (\text{Y1}, \text{Y2}); (\text{odd}, \text{even})\}$, and $\langle \dots \rangle$ implies an average over different data subsets. In the left panel of Fig. 4, we present the histogram of p_{d}^2 . The uncertainties (1σ) in p_{d}^2 are the quadratic sum of data systematic errors estimated from the three data subsets and the uncertainty in I_{G353} associated with the determination of the zero level of Galactic emission. The mean values of p_{d} over mask65 are listed in Table 1 for the different data subsets.

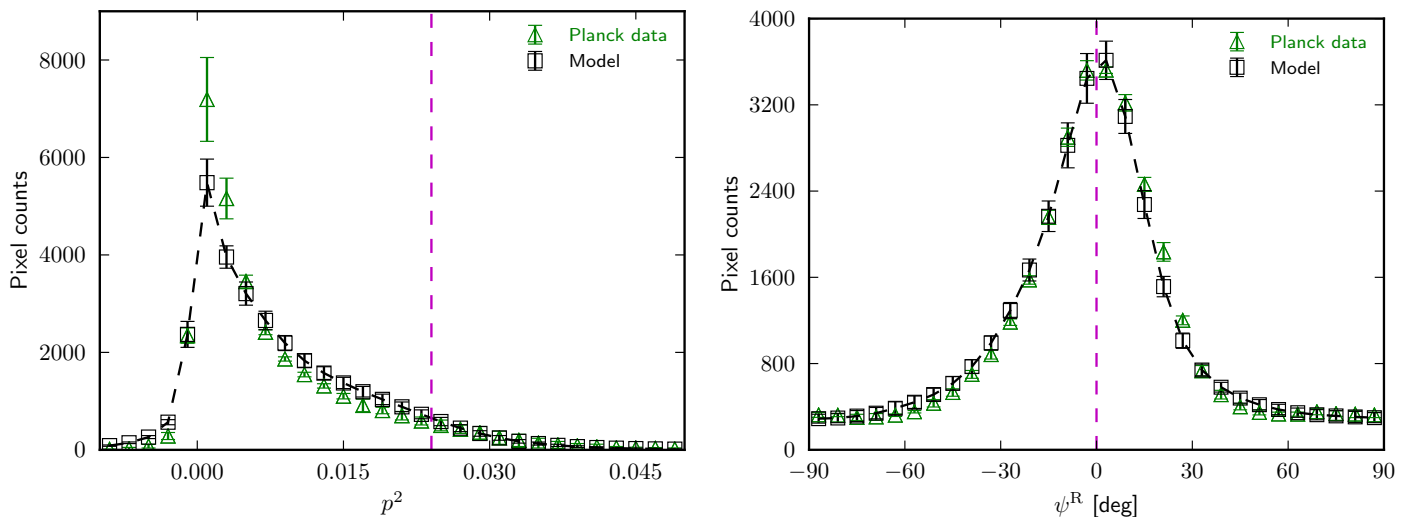


Fig. 4. *Left panel:* Histogram of the square of the polarization fraction, p^2 , at 353 GHz. *Right panel:* Histogram of ψ^R , the difference between the measured polarization angle at 353 GHz and that computed for the mean GMF orientation over mask65. *Green triangles* are mean p_d^2 (ψ_d^R) estimated from *Planck* data subsets, and *black squares* are mean p_m^2 (ψ_m^R) estimated from 100 realisations of model maps. The vertical dashed line in the *left panel* corresponds to the model parameter $p_0 = 15.5\%$ ($p_0^2 = 0.024$), while the vertical dashed line in the *right panel* corresponds to a model without a turbulent component of the GMF.

Table 1. Mean polarization fraction at 353 GHz and orientation of the large-scale GMF using different subsets of the *Planck* data.

Dataset	mean polarization fraction (p_d)	subsets	large-scale GMF l_0	b_0
Half Missions	8.8 %	HM1	61°	-17°
		HM2	64°	-19°
Years	8.8 %	YR1	61°	-17°
		YR2	64°	-19°
Odd-Even	8.8 %	odd	63°	-18°
		even	62°	-18°
Mean	–	–	62°	-18°

4.2. Polarization angle

We computed the Stokes parameter ratios, $q_d = Q_d/I_{G353}$ and $u_d = U_d/I_{G353}$ from *Planck* data at 353 GHz. As shown in the top panel of Fig. 5, maps of q_d and u_d centred at the northern Galactic pole reveal a ‘butterfly’ pattern associated with an ordered large-scale GMF.

To determine l_0 and b_0 for this large-scale GMF, we fit these data with a normalised model of Stokes parameters as described in ‘step A’ in *Planck Collaboration Int. XLIV (2016)*. The best-fit values of l_0 and b_0 for different data subsets are noted in Table 1 and the lower panel of Fig. 5 presents the best-fit model. These values, $(l_0, b_0) = (62^\circ, -18^\circ)$, give the ‘orientation’ of the GMF, but not the direction; i.e. the π ambiguity cannot be resolved using these data, though it can be resolved using rotation measures (Xu & Han 2019). The corresponding values found in TG17 for the southern Galactic cap are $(l_0, b_0) = (74^\circ, +24^\circ)$. The change of sign of b_0 from north to south reflects the deformation of the large-scale GMF by the local bubble (Alves et al. 2018).

The mean best-fit values of l_0 and b_0 are then used to calculate a polarization angle map, ψ_0 , for the mean GMF, where ψ_0

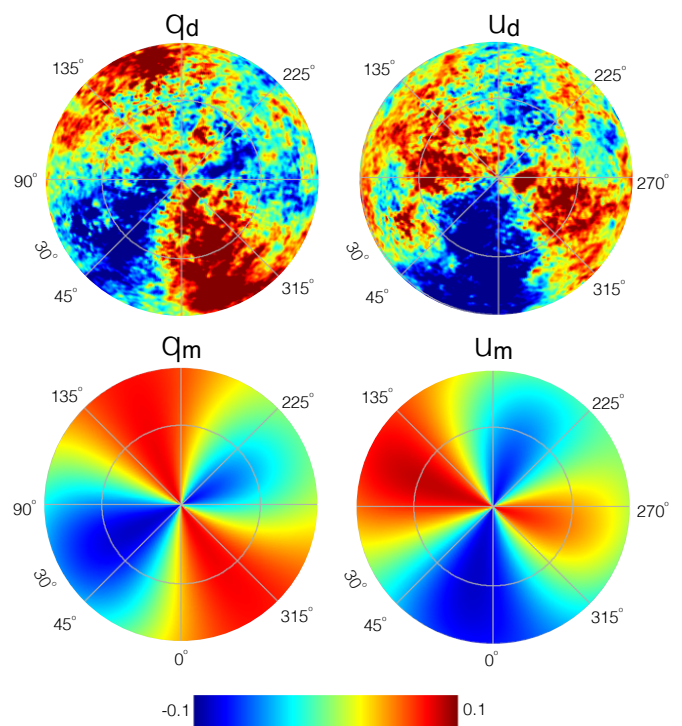


Fig. 5. *Upper panel:* Northern Galactic orthographic projection of q_d (left) and u_d (right) for the *Planck* data. *Lower panel:* Same for the best-fit model where the large-scale GMF is directed toward $(l_0, b_0) = (62^\circ, -18^\circ)$ and scaled with a mean polarization fraction of 8.8 %.

is the polarization angle of the model without the turbulent component of the GMF. At each sky pixel, we then rotate Q and U values with respect to the new reference angle ψ_0 at respective pixels using the relation,

$$\begin{bmatrix} Q_d^R \\ U_d^R \end{bmatrix} = \begin{pmatrix} \cos 2\psi_0 & -\sin 2\psi_0 \\ \sin 2\psi_0 & \cos 2\psi_0 \end{pmatrix} \begin{bmatrix} Q_d \\ U_d \end{bmatrix}, \quad (4)$$

where Q_d^R and U_d^R are Stokes parameters in the rotated frame. The polarization angle ψ_d^R is derived using the relation $\psi_d^R = 0.5 \operatorname{atan2}(-U_d^R, Q_d^R)$,

where the two-argument function $\operatorname{atan2}(-U, Q)$ is used in place of $\operatorname{atan}(-U/Q)$ to avoid the π -ambiguity. The minus sign is introduced to compute ψ_d^R in the IAU convention (Hamaker & Bregman 1996) from HEALPix maps given in the COSMO convention⁴ used by *Planck*.

Figure 4 (right panel) presents the distribution of ψ_d^R over mask65. The 1σ error bars on the distribution of ψ_d^R are computed from the standard deviation of the results from the six independent subsets of *Planck* data in Table 1. The 1σ dispersion of ψ_d^R derived from a Gaussian fit to the distribution is 16.6 ± 0.2 .

4.3. Dust power spectra

We analyse the dust polarization power spectra at 353 GHz over mask65,⁵ \mathcal{D}_ℓ^{EE} , \mathcal{D}_ℓ^{BB} , and \mathcal{D}_ℓ^{TE} , in the multipole range $40 \leq \ell \leq 160$. These were computed using Xp01 (Tristram et al. 2005) from cross spectra of three datasets: half-missions (HM1 \times HM2), years (Y1 \times Y2), and odd-even surveys (Odd \times Even). In Fig. 6, we present the mean of the three cross-power spectra in six multipole bins. The dust \mathcal{D}_ℓ^{EE} and \mathcal{D}_ℓ^{BB} spectra are corrected for CMB contributions in harmonic space using the *Planck* best-fit power spectra (Planck Collaboration VI 2018), whereas we keep \mathcal{D}_ℓ^{TE} unaltered. Uncertainties (1σ) on the binned dust power spectra are the quadratic sum of statistical noise computed by Xp01 analytically, and systematic uncertainties computed from the standard deviation from the three *Planck* data subsets.

Table 2. Fitted dust power spectra of the *Planck* data at 353 GHz and of the dust model over mask65.

Parameter	<i>Planck</i> 353 GHz data	Dust model
α_{EE}	-2.34 ± 0.16	-2.56 ± 0.18
α_{BB}	-2.51 ± 0.21	-2.56 ± 0.25
α_{TE}	-2.43 ± 0.38	-2.75 ± 0.16
$\chi_{EE}^2 (N_{d.o.f.} = 4)$	2.2	1.3
$\chi_{BB}^2 (N_{d.o.f.} = 4)$	1.8	1.3
$\chi_{TE}^2 (N_{d.o.f.} = 4)$	2.3	8.3
$A_{EE} [\mu\text{K}_{\text{CMB}}^2]$	39.1 ± 2.2	39.9 ± 2.7
$A_{BB} [\mu\text{K}_{\text{CMB}}^2]$	22.5 ± 1.6	22.0 ± 1.4
$A_{TE} [\mu\text{K}_{\text{CMB}}^2]$	74.2 ± 10.9	65.6 ± 4.0
$\langle A_{BB}/A_{EE} \rangle$	0.58 ± 0.05	0.57 ± 0.06
$\langle A_{TE}/A_{EE} \rangle$	1.90 ± 0.30	1.85 ± 0.17

We also checked the CMB correction at the map level. We subtracted the half-mission and odd-even component-separated CMB SMICA and SEVEM maps (Planck Collaboration IV 2018) from the total *Planck* maps and then computed cross-power spectra using these four subsets of the maps. Subtraction of CMB does not introduce any noticeable changes in the dust polarization power spectra.

Binned dust power spectra are well described by a power-law model, $\mathcal{D}_\ell^{XX} = A_{XX}(\ell/80)^{\alpha_{XX}+2}$, where A_{XX} is the best-fit

⁴ <https://healpix.jpl.nasa.gov/html/intronode12.htm>

⁵ $\mathcal{D}_\ell^{XX} \equiv \ell(\ell+1)C_\ell^{XX}/(2\pi)$, where $XX = EE, BB, TE$.

amplitude at $\ell = 80$, α_{XX} is the best-fit spectral index, and again $XX = \{EE, BB, TE\}$ (Planck Collaboration Int. XXX 2016). The best-fit values of A_{XX} and α_{XX} and the respective values of χ^2 are listed in the middle column of Table 2.

The ratio of BB to EE power is about 0.6 over mask65, consistent with the E - B asymmetry result of Planck Collaboration Int. XXX (2016). We detect a significant positive TE correlation over mask65, as in TG17 for the southern Galactic cap.

5. Multiphase model of polarized dust emission

We use the modelling framework from TG17, which is based on a decomposition of HI emission-line data and incorporates the phenomenological magnetic field model described in Planck Collaboration XLIV (2016). We briefly describe the salient concepts.

We use the fact that dust emission and N_{HI} are correlated so that templates of N_{HI} can be used as proxies for spatially variable dust intensity. For optically thin dust emission, the model Stokes parameters I_m , Q_m , and U_m at 353 GHz can be written as

$$\begin{aligned}
I_m(\hat{n}) &= \sum_{i=1}^N \left[1 - p_0 \left(\cos^2 \gamma^i(\hat{n}) - \frac{2}{3} \right) \right] \epsilon_{353} N_{\text{HI}}^i(\hat{n}) \\
Q_m(\hat{n}) &= \sum_{i=1}^N p_0 \cos^2 \gamma^i(\hat{n}) \cos 2\psi^i(\hat{n}) \epsilon_{353} N_{\text{HI}}^i(\hat{n}) \\
U_m(\hat{n}) &= - \sum_{i=1}^N p_0 \cos^2 \gamma^i(\hat{n}) \sin 2\psi^i(\hat{n}) \epsilon_{353} N_{\text{HI}}^i(\hat{n}),
\end{aligned} \tag{5}$$

where N is the number of distinct templates, \hat{n} is the direction vector, p_0 is a parameter related to the dust grain properties (Lee & Draine 1985; Draine & Fraisse 2009; Planck Collaboration Int. XX 2015), γ is the angle made by the local magnetic field with the plane of the sky, ψ is the polarization angle measured counterclockwise from Galactic north,⁶ ϵ_{353} is the dust emissivity at 353 GHz for each HI template, and N_{HI} is the column density within the particular template. In this work, $N = 3$, which is represented by the three distinct templates for CNM, UNM, and WNM (Sect. 3.2). This is a remarkably small number to describe the ISM. However, our focus is on demonstrating what essentials can nevertheless be captured by a polarization model that is inherently minimalist and not dependent on fine-tuning. For simplicity, ϵ_{353} is assumed to be the same for all three templates.

The connection between the dust polarization and the structure of the GMF via the angles γ and ψ is developed as in Planck Collaboration XLIV (2016). Following Jaffe et al. (2010), the GMF, \mathbf{B} , is expressed as a vector sum of an ordered component (\mathbf{B}_{ord}) and a fluctuating component (\mathbf{B}_{turb}). Because most of the dust emission comes from the thin Galactic disk, Planck Collaboration Int. XLIV (2016) assume that there is an ordered large-scale magnetic field, \mathbf{B}_{ord} , in the solar neighbourhood (approximately 200 parsec). The butterfly pattern discussed in Sect. 4.2 supports the simplifying assumption that each template has the same \mathbf{B}_{ord} , oriented toward the l_0 and b_0 that are already determined. However, the components of \mathbf{B}_{turb} are different in each template and are taken from independent realisations of a Gaussian random field that has a power spectrum with $C_\ell \propto \ell^{\alpha_M}$

⁶ IAU convention, the minus sign producing U in the COSMO convention.

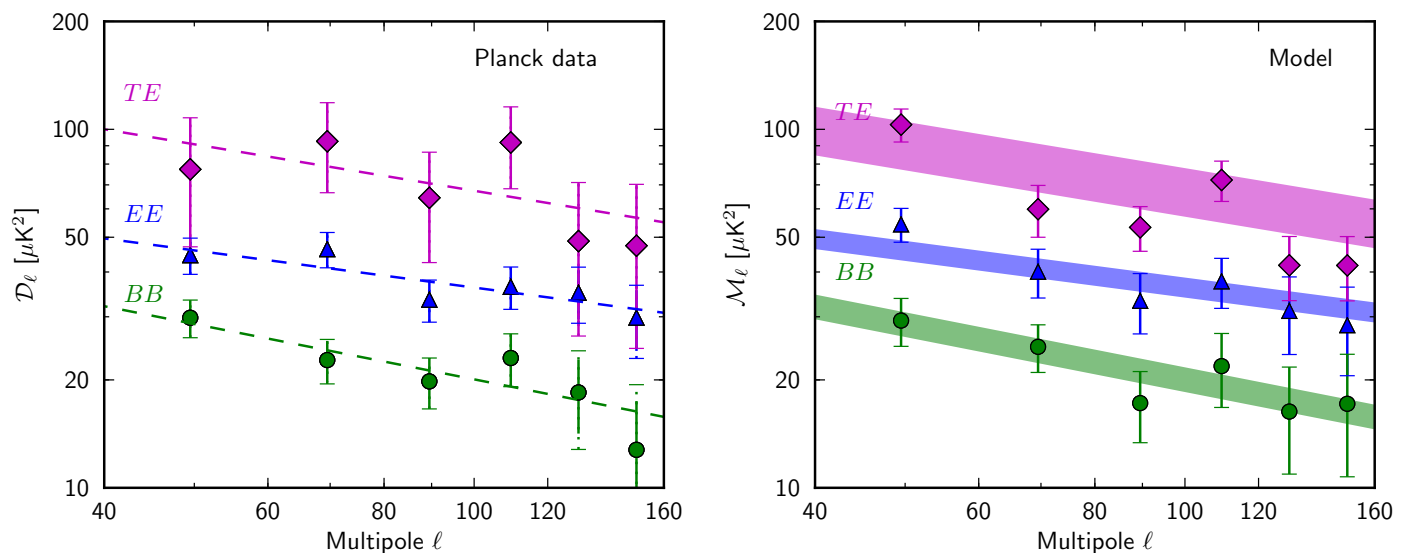


Fig. 6. *Left panel:* Dust EE , BB , and TE cross-power spectra computed from the subsets of *Planck* data at 353 GHz over mask65. *Dashed lines* represent the best-fit power laws. *Right panel:* Similar plots as *left panel* computed from 100 realisations of the dust model maps. Error bars are 1σ uncertainties as explained in the main text. The filled areas represent the *Planck* dust power spectra measurements over mask65.

for $\ell \geq 2$. The strength of $|\mathbf{B}_{\text{turb}}|$ relative to $|\mathbf{B}_{\text{ord}}|$ is parameterised by f_M^i . This phenomenological model captures schematically the association between the structure of the multiphase ISM and that of the GMF, an interdependence that we consider to be essential for modelling the dust polarization. This interdependence is usually ignored in 3D models of the GMF, for example those with Gaussian random magnetic fields as in [Levrier et al. \(2018\)](#) and [Wang et al. \(2020\)](#). However, our approach does not allow us to include the divergence-free constraint because it is not a 3D model.

Here, this key interdependence is introduced explicitly by aligning the model GMF with the structures in the HI emission maps (see section 4.3 in TG17), underlying the potential for TE correlation and E - B power asymmetry.

We can use the proxy N_{HI}^i templates as pure E -mode polarization maps, transforming them to Q and U maps and then use these latter to compute maps of the polarization angle describing the orientation. Given the evidence (Sect. 1), as in TG17, we assume alignment between the local \mathbf{B}_{POS} and dust structures represented by the CNM template and model the polarization angles ψ^c as above. However, for the UNM and WNM templates we assume no such alignment⁷ and so we apply a different procedure in which the polarization angles ψ^u and ψ^w follow from random Gaussian realisations of the components of \mathbf{B}_{turb} ([Planck Collaboration Int. XLIV 2016](#)). We simulate the $\cos^2 \gamma$ factor in Eqs. (5) along each LOS for each of three templates using the relation ([Planck Collaboration Int. XLIV 2016](#))

$$\cos^2 \gamma = 1 - |\hat{\mathbf{B}} \cdot \hat{\mathbf{r}}|^2, \quad (6)$$

where $\hat{\mathbf{B}}$ is the unit vector of total GMF and $\hat{\mathbf{r}}$ is the unit vector for a given LOS.

In summary, the seven parameters in the dust model are as follows:

⁷ In this case, there is little direct evidence for or against alignment, and again this is a minimalist approach. In the actual turbulent ISM the evolutionary relationship between gas and fields in thermal phases is complex, whether time-dependent or steady-state, and probably varies with the position because of its particular history and the ambient pressure, radiative environment, etc.

- ϵ_{353} is the mean dust emissivity at 353 GHz (all model Stokes parameters scale with this value).
- p_0 is a polarization parameter that combines the polarization degree of interstellar dust grains and their alignment efficiency.
- Galactic coordinates l_0 and b_0 determine the direction of the ordered component of the GMF.
- f_M^c parameterises the relative strength of $|\mathbf{B}_{\text{turb}}|$ and $|\mathbf{B}_{\text{ord}}|$ in the CNM template. The corresponding parameter is taken to be the same in the UNM and WNM templates and is denoted $f_M^{u/w}$.
- α_M is the exponent of the power spectrum of the turbulent component of the GMF, assumed to be the same in each template.

We simulate a set of 100 Monte-Carlo model realisations of Stokes I_m , Q_m , and U_m maps at 353 GHz for a set of parameters. Because the *Planck* data have noise, we add two independent half-mission end-to-end noise realisations provided by *Planck* ([Planck Collaboration III 2018](#)) to each noise-free dust model polarization map to produce two maps (Q and U) with independent noise. We do not add noise to the I_m maps because the I_{G353} map that we are using has negligible noise at 353 GHz.

6. Method of constraining model parameters

The best-fit orientation of \mathbf{B}_{ord} is $l_0 = 62^\circ$ and $b_0 = -18^\circ$ (see Table 1 in Sect. 4.2). Here, we describe how we fit the other five parameters of the model.

6.1. Turbulent magnetic field in the CNM template

From the N_{HI}^c template we compute the polarization angles using the method described in Sect. 5. In particular, we compute maps of $\cos 2\psi^c$. In the CNM the assumed alignment of the local GMF with respect to the gas structures constrains the pair of parameters, f_M^c and α_M , that characterise \mathbf{B}_{turb} .

To evaluate these constraints, following TG17 we simulate $\cos 2\psi$ for different values of the pairs assuming the adopted

orientation of \mathbf{B}_{ord} , using algebra described in section 4.1 of [Planck Collaboration Int. XLIV \(2016\)](#). For each pair, we compute means of power spectrum amplitudes of $\cos 2\psi$ from 100 Monte-Carlo realisations over mask65 and fit these with a power-law model $\mathcal{D}_\ell \propto \ell^{\alpha_M+2}$ within multipole range $40 \leq \ell \leq 160$ (Fig. 7). Comparing the power spectra of the $\cos 2\psi^c$ map with the simulated spectra of $\cos 2\psi$ for different pairs of f_M and α_M , we adopt the following pair of parameter values for the CNM template: $f_M^c = 0.5_{-0.04}^{+0.05}$ and $\alpha_M = -2.4 \pm 0.1$.

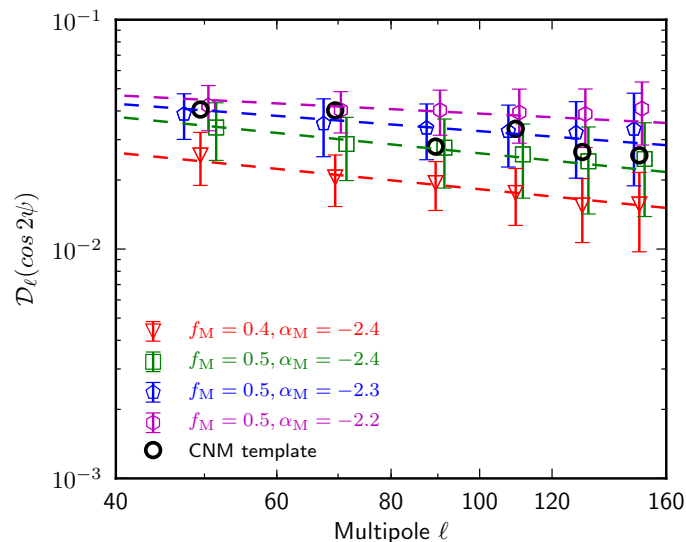


Fig. 7. Means of power spectrum amplitudes from simulated model maps of $\cos 2\psi$ within the multipole range $40 \leq \ell \leq 160$ for different values of f_M and α_M and the best-fit power laws (dashed lines). The error bars (1σ) are standard deviations computed from 100 realisations. Black circles are power spectrum amplitudes from the map of $\cos 2\psi^c$ computed from the CNM template.

Applying the same procedure to the UNM and WNM templates results in a value of $f_M^{\text{u/w}}$ much higher than f_M^c for the CNM template. However, as seen next, the model fit does not support such high turbulence in the UNM or WNM. As discussed in Sect. 6.2, the model is in favour of a very low turbulence in both the UNM and WNM, with $f_M^{\text{u/w}} = 0.1$.

6.2. Additional model parameters

We determine the three remaining model parameters, ϵ_{353} , p_0 , and $f_M^{\text{u/w}}$, by jointly minimising the following two expressions for χ^2 . One is in harmonic space (Fig. 6, Table 2):

$$\chi_{XX}^2 = \sum_{\ell_{\min}}^{\ell_{\max}} \left[\frac{\mathcal{D}_\ell^{XX} - \mathcal{M}_\ell^{XX}(\epsilon_{353}, p_0, f_M^{\text{u/w}})}{\sigma_\ell^{XX}} \right]^2, \quad (7)$$

where $XX = \{EE, BB, TE\}$, \mathcal{D}_ℓ^{XX} and \mathcal{M}_ℓ^{XX} are binned power spectra of dust within the multipole range $40 \leq \ell \leq 160$ for the data and model, respectively, and σ_ℓ^{XX} are the corresponding standard deviations. The other is in pixel space (Fig. 8):

$$\chi^2 = \sum_{i=1}^{N_{\text{pix}}} \left[I_{G353} - sI_m(\epsilon_{353}, p_0, f_M^{\text{u/w}}) - o \right]^2. \quad (8)$$

Through combining statistics of the polarized dust observations in both harmonic and pixel space, we break the degeneracy between the two model parameters ϵ_{353} and p_0 in Eq. (5). The χ^2

of the T–T correlation between I_{G353} and I_m is minimised in pixel space over mask65. To match the observed dust amplitude at 353 GHz, the value of s should be close to 1 and is kept so by adjusting ϵ_{353} during the iterative solution of the two equations.

The best-fit values are $\epsilon_{353} = 146 \mu\text{K}_{\text{CMB}}(10^{20} \text{ cm}^{-2})^{-1}$, $p_0 = 15.5\%$, and $f_M^{\text{u/w}} = 0.1$. Compared to the values of ϵ_{353} and p_0 found by TG17 in their analysis of the southern Galactic cap, our values differ by factors of 1.2 and 0.84, respectively.

7. Comparison of the model with *Planck* observations

Using the methods detailed in Sect. 6, we determined parameters of the Stokes dust model such that several statistical properties computed from the model match the *Planck* dust observations at 353 GHz over mask65 in both pixel and harmonic space. The quality of these matches to constraining the *Planck* polarization data is demonstrated below. Furthermore, we show in Sect. 8 that the dust model is able to reproduce the observed inverse relationship between the polarization angle dispersion and the polarization fraction over mask65, even though these statistics were not used in determining the model parameters.

7.1. Polarization fraction

We compute the mean square of the polarization fraction, p_m^2 , from 100 realisations using Eq. (5). The error bars on the mean histogram are the standard deviations estimated over the 100 realisations. As shown in Fig. 4 (left), our model reproduces the statistical distribution of p_d^2 quite accurately, including the negative values of p_d^2 and the largest values beyond p_0^2 .

7.2. Polarization angle

We compute the polarization angle, ψ_m^R , from 100 realisations of the model, following the method described in Sect. 4.2 and used for the data. For each sky realisation i , we fit the ordered component of GMF using l_0^i and b_0^i and from the map of the mean polarization angle of the GMF ψ_0^i . At each sky pixel in the realisation of the Stokes model maps we then rotate Q_i and U_i with respect to the new reference angle ψ_0^i at respective pixels using Eq. (4). The polarization angle ψ_i^R is then derived from the rotated Q_i and U_i maps. The mean polarization angle, ψ_m^R , for the model is computed by taking the mean of the histograms of ψ_i^R distributions for each bin. Similarly, the uncertainties for each bin of the histogram are computed from the standard deviation of 100 realisations. As shown in Fig. 4 (right), our model reproduces the statistical distribution of ψ_d^R . The dispersion of ψ_m^R derived from a Gaussian fit is $17^\circ.5 \pm 0^\circ.4$, which is slightly higher than that for the data ψ_d^R : $16^\circ.6 \pm 0^\circ.2$. The difference might come from the fact that the model is not fitted to the *Planck* data at $\ell < 40$, which cannot be accomplished accurately over the limited area of mask65.

7.3. Dust polarization spectra

We compute mean cross-power spectra from 100 sets of two independent realisations of the Stokes model maps. We fit the binned power spectra with power laws: $\mathcal{M}_\ell^{XX} = A_{XX}(\ell/80)^{\alpha_{XX}+2}$ within the multipole range $40 \leq \ell \leq 160$. Error bars in each bin are the standard deviations computed from 100 realisations. Best-fit amplitudes, A_{XX} and exponents, α_{XX} along with the corresponding χ^2 values, are listed in the right

column of Table 2. We compare the results with the *Planck* dust power spectra in Fig. 6. The \mathcal{D}_ℓ^{EE} and \mathcal{D}_ℓ^{BB} amplitudes and their ratio match the values from the data accurately. The \mathcal{D}_ℓ^{TE} amplitude for the dust model is slightly lower, but consistent with the *Planck* data within its uncertainty.

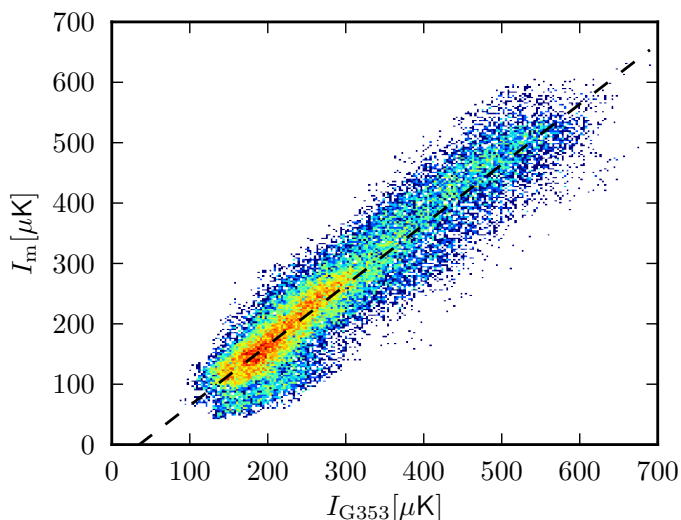


Fig. 8. Correlation plot between I_m and I_{G353} at 353 GHz. The black dashed line is the result of the joint optimisation of Eqs. (7) and (8).

7.4. Total intensity

Figure 8 shows the tight correlation between I_m and I_{G353} at 353 GHz, which demonstrates that statistically, the model dust intensity reproduces the observed *Planck* dust intensity. The best-fit dashed line shown has slope $s = 1.0$ and offset $o = -35 \mu\text{K}_{\text{CMB}}$, again within the uncertainty of the zero level in the intensity, $40 \mu\text{K}_{\text{CMB}}$ (Sect. 2.1).

8. Inverse relationship between the polarization angle dispersion and the polarization fraction

The polarization angle dispersion function, \mathcal{S} , was introduced in *Planck Collaboration Int. XIX (2015)* to quantify the local dispersion of the dust polarization angle for a given angular resolution and lag δ . An inverse relationship between \mathcal{S} and p_{MAS} was found, where p_{MAS} is the modified asymptotic estimator of the polarization fraction (*Plaszczynski et al. 2014*). That analysis was done over 42% of the sky at low and intermediate Galactic latitudes at a resolution of 1° (FWHM) with a lag $\delta = 30'$. *Planck Collaboration XII (2018)* extended this work over the full sky using GNILC processed intensity and polarization maps at a resolution of $160'$ (FWHM) with $\delta = 80'$ and found that $\mathcal{S} \propto p_{\text{MAS}}^{-1}$.

Here, we study the relationship between \mathcal{S} and p_{MAS} over mask65 using 353 GHz maps at a resolution of $80'$ (FWHM) with $\delta = 40'$. The noise bias parameter needed for p_{MAS} (*Montier et al. 2015a,b*) is estimated from the smoothed noise covariance matrices, $\sigma_{II}, \sigma_{IQ}, \sigma_{IU}, \sigma_{QQ}, \sigma_{QU}, \sigma_{UU}$ at a resolution of $80'$ (FWHM) and $N_{\text{side}} = 128$.

In the *top panel* of Fig. 9, we present the two-dimensional joint distribution of \mathcal{S} and p_{MAS} for the *Planck* data over mask65. The running mean of \mathcal{S} in each bin of p_{MAS} follows an inverse relationship, $\mathcal{S} = (0.43 \pm 0.04)/p_{\text{MAS}}$. In the

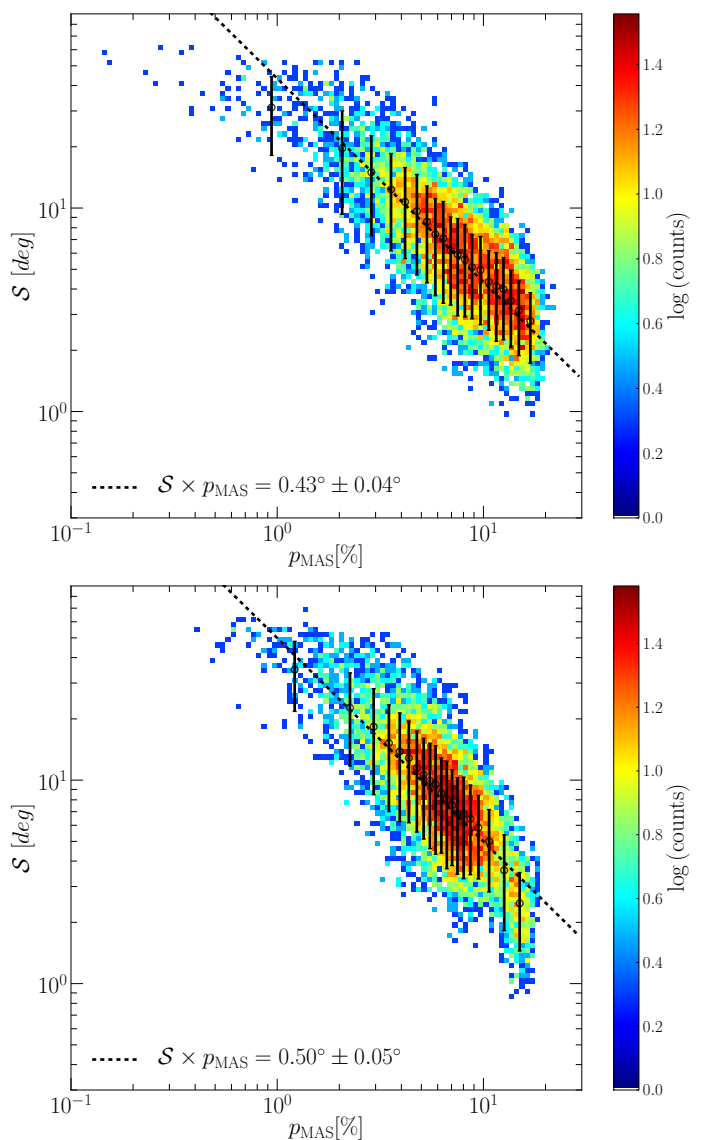


Fig. 9. *Top panel:* Two-dimensional histogram of the joint distribution of \mathcal{S} and p_{MAS} over mask65 for the *Planck* data at a resolution of $80'$ with lag $\delta = 40'$. The black circles show the mean of \mathcal{S} in bins of p_{MAS} containing the same number of map pixels. Error bars are the standard deviation of \mathcal{S} in each bin. The black dotted line is a fit of the running mean. *Bottom panel:* Same as *top panel*, but for the model.

bottom panel of Fig. 9, we show the corresponding $\mathcal{S} - p_{\text{MAS}}$ distribution for our model. This too has an inverse relationship and the slope 0.50 ± 0.05 is very close to that for the *Planck* data. This is remarkable given that this statistical property of dust polarization has not been exploited in the fit of our model parameters.

9. Summary and Discussion

In this paper, we analyse the statistical properties of the *Planck* dust polarization maps at 353 GHz at a $60'$ resolution (FWHM) over a low-column-density region that accounts for 65% of the northern Galactic cap at latitudes larger than 30° (mask65). We make use of the multiphase dust polarization model described in TG17. The model shows how the dust polarization across the sky can be approximated on the basis of proxy HI data: in particular, three independent templates notionally representing the contri-

butions from the CNM, UNM, and WNM. The model has seven adjustable parameters whose values are determined by reproducing *Planck* observations at 353 GHz: in particular, the one-point statistics of p and ψ in pixel space, and the EE , BB , and TE power spectra in harmonic space. Our main results can be summarised as follows.

- The butterfly pattern seen in q_d and u_d maps (Fig. 5) around the pole is associated with an ordered GMF, which we find has a mean orientation in Galactic coordinates toward $(l_0, b_0) = (62^\circ, -18^\circ)$ (Sect. 4.2). The best-fit value of l_0 is roughly consistent with the earlier values derived from starlight polarization (Ellis & Axon 1978; Heiles 1996).
- From the *Planck* data, we find a BB/EE power ratio of 0.58 and significant positive TE correlation over mask65 (Sect. 4.3). The key property in our model that allows the model to reproduce these observations (Sect. 7.3) is the alignment of the local magnetic field \mathbf{B}_{POS} and the HI structure in the CNM template (Sect. 5).
- The observed distributions of p and ψ over mask65 show a scatter that is comparable to that of the distributions reported for the whole sky in *Planck Collaboration XII* (2018). Our model successfully reproduced these one-point statistics associated with LOS depolarization (Sects. 7.1 and 7.2) by introducing fluctuations in the GMF orientation that are uncorrelated between the three independent HI templates (Sect. 3.2).
- The best-fit value of the parameter, p_0 , that measures the grain alignment efficiency combined with the intrinsic polarization fraction of interstellar dust emission at 353 GHz, is 15.5%. The best-fit value of the dust emissivity is $\epsilon_{353} = 146 \mu\text{K}_{\text{CMB}} (10^{20} \text{ cm}^{-2})^{-1}$ (Sect. 6.2).
- To match the observed EE , BB , and TE amplitudes, the model fit yields a low value of the parameter $f_M^{u/w}$ specifying the relative amplitude of the turbulent component of the GMF in the UNM and WNM. This value, 0.1, is significantly smaller than the value $f_M^c = 0.5$ characterising the CNM (Sect. 6.1).
- The spectral index of the turbulent component of the GMF, $\alpha_M = -2.4$, fitted over mask65 (Sect. 6.1), is consistent with the value reported in TG17. These two complementary analyses reveal that the spectral index of turbulent magnetic field closely matches the power-law index of dust polarization power spectra, as expected.
- Our model also reproduces the inverse relationship between the polarization angle dispersion, \mathcal{S} , and the polarization fraction, p_{MAS} , present in the *Planck* data, despite the fact that we do not utilise this phenomenon in fitting the model parameters (Sect. 8). Our work reinforces the conclusion in *Planck Collaboration XII* (2018) that the inverse relationship of \mathcal{S} and p_{MAS} is a generic feature associated with the GMF structure.

This work demonstrates that the phenomenological model introduced in TG17 for the southern Galactic cap also works well in the northern hemisphere. The next step in our modelling work will be to extend this framework to multiple frequencies by incorporating spectral energy distributions for the dust emission associated with the three HI templates thus introducing the potential for frequency decorrelation of the dust polarization. This is a necessary step towards investigating the utility of this framework for evaluating component separation methods for future CMB missions.

Acknowledgements. We gratefully acknowledge the use of the Aquila cluster at NISER, Bhubaneswar. DA acknowledges the University Grants Commission India for providing financial support as Senior Research Fellow. This work was supported by the Science and Engineering Research Board, Department of Science and Technology, Govt. of India grant number SERB/ECR/2018/000826 and the Natural Sciences and Engineering Research Council of Canada. Some of the results in this paper have been derived using the HEALPix package. The *Planck* Legacy Archive (PLA) contains all public products originating from the *Planck* mission, and we take the opportunity to thank ESA/*Planck* and the *Planck* collaboration for the same. This work has made use of HI data of the EBHIS survey headed by the Argelander-Institut für Astronomie (PI J. Kerp) in collaboration with the Max-Planck-Institut für Radioastronomie and funded by the Deutsche Forschungsgemeinschaft (grants KE757/7-1 to 7-3). The Gaussian decomposition of the EBHIS data was supported by the Estonian Research Council grant IUT26-2, and by the European Regional Development Fund (TK133).

References

- Alves, M. I. R., Boulanger, F., Ferrière, K., & Montier, L. 2018, *A&A*, 611, L5
 Andersson, B. G., Lazarian, A., & Vaillancourt, J. E. 2015, *Annual Review of Astronomy and Astrophysics*, 53, 501
 Arendt, R. G., Odegard, N., Weiland, J. L., et al. 1998, *ApJ*, 508, 74
 Ashton, P. C., Ade, P. A. R., Angilè, F. E., et al. 2018, *ApJ*, 857, 10
 Caldwell, R. R., Hirata, C., & Kamionkowski, M. 2017, *The Astrophysical Journal*, 839, 91
 Clark, S. E. 2018, *ApJ*, 857, L10
 Clark, S. E. & Hensley, B. S. 2019, *ApJ*, 887, 136
 Clark, S. E., Hill, J. C., Peek, J. E. G., Putman, M. E., & Babler, B. L. 2015, *Phys. Rev. Lett.*, 115, 241302
 Clark, S. E., Peek, J. E. G., & Miville-Deschênes, M. A. 2019, *ApJ*, 874, 171
 Clark, S. E., Peek, J. E. G., & Putman, M. E. 2014, *The Astrophysical Journal*, 789, 82
 Davis, Jr., L. & Greenstein, J. L. 1951, *ApJ*, 114, 206
 Draine, B. T. & Fraisse, A. A. 2009, *The Astrophysical Journal*, 696, 1
 Draine, B. T. & Fraisse, A. A. 2009, *ApJ*, 696, 1
 Ellis, R. S. & Axon, D. J. 1978, *Ap&SS*, 54, 425
 Fabbri, R. & Pollock, M. 1983, *Physics Letters B*, 125, 445
 Ghosh, T., Boulanger, F., Martin, P. G., et al. 2017, *A&A*, 601, A71
 Gillmon, K., Shull, J. M., Tumlinson, J., & Danforth, C. 2006, *ApJ*, 636, 891
 Górski, K. M., Hivon, E., Banday, A. J., et al. 2005, *ApJ*, 622, 759
 Hamaker, J. P. & Bregman, J. D. 1996, *A&AS*, 117, 161
 Haud, U. 2000, *A&A*, 364, 83
 Haud, U. 2013, *A&A*, 552, A108
 Heiles, C. 1996, *ApJ*, 462, 316
 HI4PI Collaboration, Ben Bekhti, N., Flöer, L., et al. 2016, *A&A*, 594, A116
 Hivon, E., Górski, K. M., Netterfield, C. B., et al. 2002, *ApJ*, 567, 2
 Jaffe, T. R., Leahy, J. P., Banday, A. J., et al. 2010, *MNRAS*, 401, 1013
 Jow, D. L., Hill, R., Scott, D., et al. 2018, *MNRAS*, 474, 1018
 Kalberla, P. M. W. & Haud, U. 2018, *A&A*, 619, A58
 Kalberla, P. M. W., Kerp, J., Haud, U., et al. 2016, *ApJ*, 821, 117
 Kandel, D., Lazarian, A., & Pogogyan, D. 2017, *MNRAS*, 472, L10
 Kandel, D., Lazarian, A., & Pogogyan, D. 2018, *Monthly Notices of the Royal Astronomical Society*, 478, 530
 Kerp, J., Winkel, B., Ben Bekhti, N., Flöer, L., & Kalberla, P. M. W. 2011, *Astronomische Nachrichten*, 332, 637
 Lazarian, A. 2007, *Journal of Quantitative Spectroscopy and Radiative Transfer*, 106, 225
 Lee, H. M. & Draine, B. T. 1985, *ApJ*, 290, 211
 Levrier, F., Neveu, J., Falgarone, E., et al. 2018, *A&A*, 614, A124
 Martin, P. G. 2007, *EAS Publications Series*, 23, 165
 Martin, P. G., Blagrove, K. P. M., Lockman, F. J., et al. 2015, *ApJ*, 809, 153
 Montier, L., Plaszczynski, S., Levrier, F., et al. 2015a, *A&A*, 574, A135
 Montier, L., Plaszczynski, S., Levrier, F., et al. 2015b, *A&A*, 574, A136
 Planck Collaboration XLIV. 2016, *A&A*, 596, A105
 Planck Collaboration XXIV. 2011, *A&A*, 536, A24
 Planck Collaboration XI. 2014, *A&A*, 571, A11
 Planck Collaboration I. 2016, *A&A*, 594, A1
 Planck Collaboration I. 2018, *A&A*, in press [arXiv:1807.06205]
 Planck Collaboration III. 2018, *A&A*, in press [arXiv:1807.06207]
 Planck Collaboration IV. 2018, *A&A*, in press [arXiv:1807.06208]
 Planck Collaboration VI. 2018, *A&A*, in press [arXiv:1807.06209]
 Planck Collaboration XI. 2018, *A&A*, in press [arXiv:1801.04945]
 Planck Collaboration XII. 2018, *A&A*, in press [arXiv:1807.06212]
 Planck Collaboration Int. XVII. 2014, *A&A*, 566, A55
 Planck Collaboration Int. XIX. 2015, *A&A*, 576, A104
 Planck Collaboration Int. XX. 2015, *A&A*, 576, A105
 Planck Collaboration Int. XXII. 2015, *A&A*, 576, A107
 Planck Collaboration Int. XXX. 2016, *A&A*, 586, A133

- Planck Collaboration Int. XXXII. 2016, A&A, 586, A135
Planck Collaboration Int. XXXV. 2016, A&A, 586, A138
Planck Collaboration Int. XXXVIII. 2016, A&A, 586, A141
Planck Collaboration Int. XLIV. 2016, A&A, 596, A105
Plaszczynski, S., Montier, L., Levrier, F., & Tristram, M. 2014, MNRAS, 439, 4048
Remazeilles, M., Dickinson, C., Eriksen, H. K. K., & Wehus, I. K. 2016, MNRAS, 458, 2032
Savage, B. D., Bohlin, R. C., Drake, J. F., & Budich, W. 1977, ApJ, 216, 291
Soler, J. D., Ade, P. A. R., Angilè, F. E., et al. 2017, A&A, 603, A64
Soler, J. D., Hennebelle, P., Martin, P. G., et al. 2013, ApJ, 774, 128
Starobinskij, A. A. 1979, Pisma v Zhurnal Eksperimentalnoi i Teoreticheskoi Fiziki, 30, 719
Stein, W. 1966, ApJ, 144, 318
Tristram, M., Macías-Pérez, J. F., Renault, C., & Santos, D. 2005, MNRAS, 358, 833
Vaillancourt, J. E. & Matthews, B. C. 2012, The Astrophysical Journal Supplement Series, 201, 13
Wang, J., Jaffe, T. R., Ensslin, T. A., et al. 2020, ApJS, 247, 18
Wilson, T. L., Rohlf, K., & Hüttemeister, S. 2009, Tools of Radio Astronomy (Springer-Verlag)
Winkel, B., Kerp, J., Flöer, L., et al. 2016, A&A, 585, A41
Xu, J. & Han, J. L. 2019, MNRAS, 486, 4275

Appendix A: Analysis with an alternative set of HI templates

Here we describe the development of an alternative set of HI templates and then the results from a modelling analysis similar to that presented in the main paper.

Kalberla & Haud (2018) (hereafter KH18) performed a Gaussian decomposition of EBHIS HI emission spectra from an intermediate product of the HI4PI all-sky survey (HI4PI Collaboration et al. 2016), applying the algorithm described in Haud (2000) with some modifications (see their section 2.2). Based on line widths, KH18 defined HI components called the cold, luke-warm, and warm neutral medium (CNM, LNM, and WNM, respectively). The separation was done using intervals of line width or the corresponding Doppler temperature (T_D), which depend on $|v|$ (see, e.g. their figures 3 and 7). For example, for velocities $|v| \leq 8 \text{ km s}^{-1}$ over the full sky, the mean line widths are 3.6, 9.6, and 23.3 km s^{-1} FWHM for the CNM, LNM, and WNM components, respectively.

Making use of this Gaussian decomposition, we consider here Gaussian components whose central peak velocity v_c^i lies within the velocity range of $|v_c| \leq 24 \text{ km s}^{-1}$, which encompasses most of the local HI gas (Kalberla & Haud 2018) but ignores most intermediate velocity gas (IVC). This decomposition was done at the native resolution in maps with $N_{\text{side}} = 1024$. As in Kalberla & Haud (2018), maps of the integrated emission of HI were made for the CNM, LNM, and WNM components at an angular resolution of $30'$ (FWHM). For our alternative analysis, these column density maps were further smoothed to $60'$ (FWHM) and downgraded to $N_{\text{side}} = 128$. The smoothing reduces uncertainties within each map that arise from separating the gas into components. These maps are shown in Fig. A.1. Hereafter, we refer to these as the KH18 templates.

We refer to the sum of the column densities of the three templates as $N_{\text{HI},24}$. The correlation of dust emission with $N_{\text{HI},24}$ on the selected region mask65 is not satisfactory, having an emissivity $\epsilon_{353,24}$ of $121 \mu\text{K}_{\text{CMB}}(10^{20} \text{ cm}^{-2})^{-1}$, lower than $\epsilon_{353,50}$, and also an unacceptably large offset, $115 \mu\text{K}_{\text{CMB}}$. This arises because of the restricted velocity range adopted from KH18: $N_{\text{HI},24} \leq N_{\text{HI},50}$ and is not an adequate proxy for all of the dust. Therefore, to make the model more rigorous we introduced an additional fourth template to compensate for the missing HI. The fourth template is simply the column density map $N_{\text{HI},50} - N_{\text{HI},24}$, also shown in Fig. A.1.

The sum of the KH18 CNM and LNM templates is related to our CNM template used in the main paper, as shown in Fig. A.2. The slope of the pixel by pixel correlation between the sum of the KH18 CNM and LNM templates and our CNM template is 1.02 over mask65, which confirms that CNM and LNM from KH18 can be considered embedded in the gas in our CNM template. Therefore, in building this alternative model we assume that the local \mathbf{B}_{POS} of the model GMF is aligned with HI structures in both of the CNM and LNM templates of KH18 (Sect. 5).

Applying the technique discussed in Sect. 6.1, we find $f_M^c = 0.5$ and $\alpha_M = -2.4$ (see Fig. A.3). Because the error bars on $\cos 2\psi$ estimated from simulated maps are significant, on the basis of Fig. A.3 we adopt the same pair of parameter values for the LNM. In the WNM, we adopt f_M^w a lower value, 0.1. The fourth template is assumed to be unpolarized. For these alternative templates, the other three parameters optimised (Sect. 6.2) are $\epsilon_{353} = 146 \mu\text{K}_{\text{CMB}}(10^{20} \text{ cm}^{-2})^{-1}$ and $p_0 = 19\%$.

Within our multiphase dust modelling framework (Sect. 5), these seven parameters and four templates can reproduce (Sect. 7) all of the observed statistical properties of dust (Sect. 4)

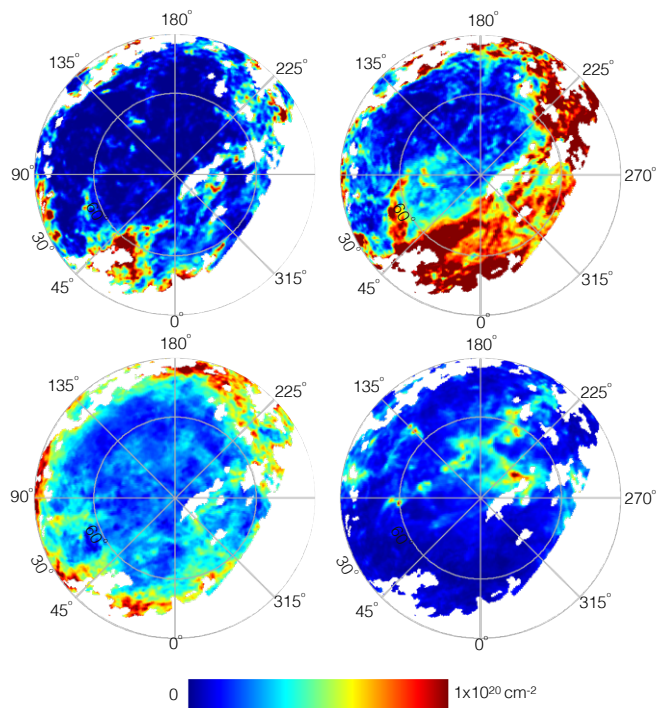


Fig. A.1. Northern Galactic orthographic projection of N_{HI} of the three KH18 templates, CNM (upper left), LNM (upper right), and WNM (lower left), and the additional fourth template (lower right) over our selected region mask65 (Sect. 3.1). The mean column densities of the four templates are $\langle N_{\text{HI}}^c \rangle = 0.19 \times 10^{20} \text{ cm}^{-2}$, $\langle N_{\text{HI}}^l \rangle = 0.52 \times 10^{20} \text{ cm}^{-2}$, $\langle N_{\text{HI}}^w \rangle = 0.75 \times 10^{20} \text{ cm}^{-2}$, and $\langle N_{\text{HI}}^{4\text{th}} \rangle = 0.37 \times 10^{20} \text{ cm}^{-2}$, respectively.

quite well, including the power spectra as shown in Fig. A.4. For ℓ bins between 40 and 160, the alternative set of HI templates is able to produce dust EE and BB power spectra with similar strength as the *Planck* data. The overall BB power is at the right level and the BB/EE ratio is about 0.57.

However, the predicted TE is an exception. There are two concerns. First, the overall level of the TE power across most scales is low relative to the *Planck* data (shown originally in Fig. 6 left). Second, the pattern of ℓ -dependent deviations from a smooth power-law dependence is more pronounced compared to our model in Fig. 6. These deviations could come from excess small-scale power in the KH18 CNM or LNM templates that corrupts the TE (and EE) power spectra at small scales.

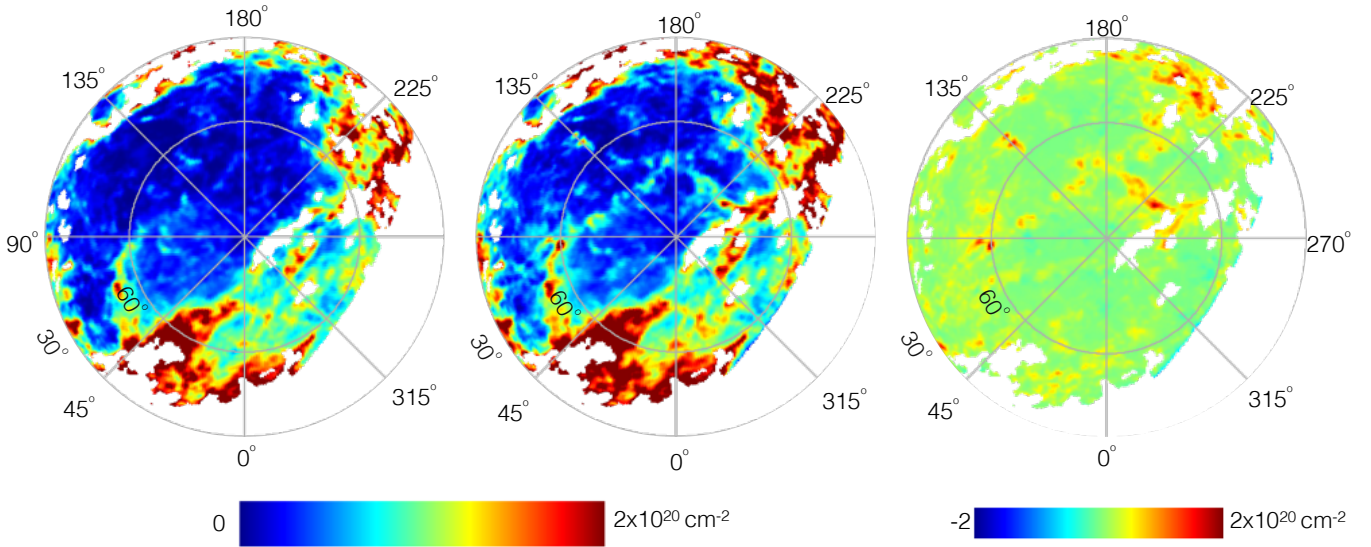


Fig. A.2. Northern Galactic orthographic projection of our CNM template (*left panel*), the KH18 CNM plus LNM templates (*middle panel*), and the difference between the two (*right panel*).

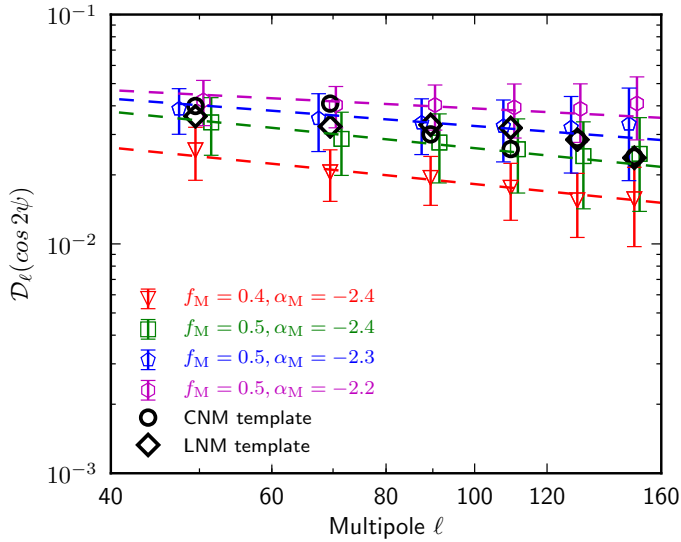


Fig. A.3. Mean of simulated power spectra of $\cos 2\psi$ within the multipole range $40 \leq \ell \leq 160$ for different values of f_M and α_M and best fit power-law (*dashed lines*). The error-bars (1σ) are standard deviations computed from 100 realisations. *Black circles* and *black diamonds* are power spectra of $\cos 2\psi$ computed (Sect. 3.2) from the CNM and LNM templates of KH18.

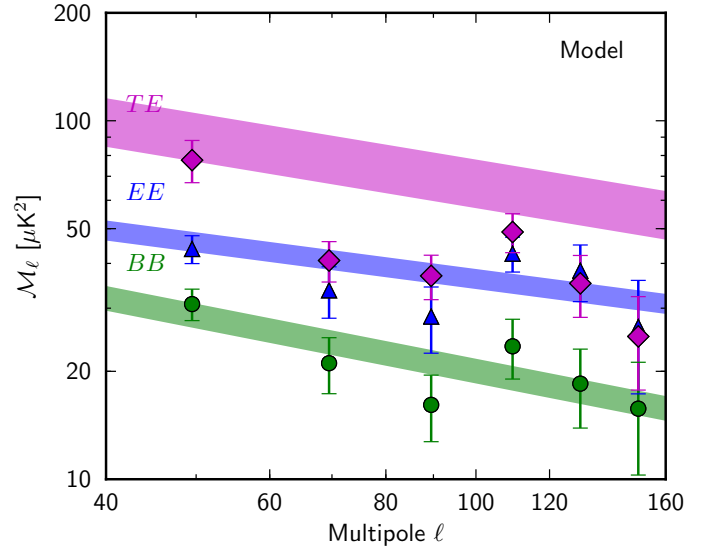


Fig. A.4. Dust EE , BB , and TE cross-power spectra in units of $\mu\text{K}_{\text{CMB}}^2$ computed from the subsets of 100 realisations of the dust model maps over mask65 using the CNM, LNM, and WNM of KH18 and the fourth template. The filled areas represent the *Planck* dust power spectra measurements over mask65 computed in Sect. 4.3.